Dalton Transactions

ROYAL SOCIETY OF CHEMISTRY

PAPER

View Article Online
View Journal | View Issue

Cite this: *Dalton Trans.*, 2025, **54**, 8287

Synthesis of Fe-zeolites from Amazonian kaolinite for methylene blue removal: adsorption and photocatalytic activity

Victor Augusto Araújo de Freitas, *[a] Débora de Souza Pinheiro,[a] Camila Ferreira Peixoto,[a] Luiz Carlos Alves de Oliveira[b] and Paulo Rogério da Costa Couceiro[c]

Zeolites exhibit high adsorption capacities for organic substrates and catalytic activity owing to their unique structural features, such as uniform pore sizes and Lewis acidity. However, their inherent UV-vis transparency (λ > 240 nm) limits their efficacy as photocatalysts. This limitation can be addressed by incorporating transition metals into their framework or encapsulating semiconductors within their porous structures. In this study, Fe-zeolites were synthesized through alkaline fusion of natural Amazonian kaolinite, followed by hydrothermal treatment with varying Fe^{3+} loadings from $Fe(NO_3)_3$. In the absence of $Fe(NO_3)_3$, an LTA zeolite was obtained under these experimental conditions. However, the introduction of $Fe(NO_3)_3$ led to the formation of a cancrinite (CAN) zeolite, suggesting that nitrate anions acted as a structure-directing agent. XRD and Mössbauer spectroscopy confirmed the presence of Fe-doped cancrinite and dispersed maghemite within FeZEO-3 and FeZEO-5. Methylene blue adsorption onto Fe-zeolites was best described using the Langmuir isotherm model and followed pseudo-second-order kinetics. An increase in iron content from 0 to 5% (w/w) led to enhanced photoactivity, as evidenced by a decrease in band gap energy from 3.21 eV to 2.93 eV and finally to 2.53 eV. This improved photoactivity was further supported by the observation of hydroxylated methylene blue intermediates during the photocatalysis process as the FeZEO-5 material removed up to 90% of the dye.

Received 21st February 2025,
Accepted 7th April 2025

DOI: 10.1039/d5dt00439j

rsc.li/dalton

1 Introduction

Zeolites are crystalline aluminosilicates composed of a three-dimensional framework of interconnected silicon (SiO_4) and aluminum (AlO_4^-) tetrahedra. The diverse arrangement possibilities of these tetrahedra result in over 200 distinct crystal structures with special properties (such as porous structures, ion exchange capabilities, and catalytic activity), which enables their application in the petrochemical industry, gas separation, detergent builders, and water treatment.[1–3]

Most of the commercial zeolites are synthetic since the synthesis process allows a fine control of the crystallinity, porosity and purity of the zeolitic product. However, the synthesis routes use pure chemical raw materials (sodium silicate, silica, aluminum sulfate and sodium aluminate), which may represent a drawback in their application from an environmental perspective. Therefore, the development of synthesis routes for zeolitic materials using cost-effective raw materials is a constant demand for the scientific community.[1,4,5]

Rice husk ash, coal fly ash, and red mud, being industrial solid residues with a high silicon content, have been extensively studied as potential zeolitic precursors due to their abundant production. Most studies utilizing these precursors focus on synthesizing zeolite A (LTA) and zeolite X (FAU), although zeolite P (GIS), sodalite (SOD), and analcime (ANA) often emerge as secondary or undesired zeolitic phases. Despite the success in utilizing these waste materials, the addition of aluminum sulfate is necessary due to their deficiency in aluminum, a crucial component for zeolite synthesis.[1]

Clay minerals, such as kaolinite, illite, bentonite, and montmorillonite, are abundant natural silica-aluminate materials resulting from soil weathering or rock-formation processes.[6] Kaolinite has an ideal chemical composition of $Al_2O_3{\cdot}2SiO_2{\cdot}2H_2O$ and can be found with high purity in large kaolin reserves. It is a layered silicate mineral type 1 : 1, which denotes a structure composed of a sheet of silica tetrahedra

[a]*Departamento de Ciências Naturais, Universidade Federal de São João del Rei, Brazil. E-mail: victorfreitas@ufsj.edu.br; Tel: +55-32-999066079*
[b]*Departamento de Química, Universidade Federal de Minas Gerais. Av. Pres. Antônio Carlos, 6627 – Pampulha, Belo Horizonte – MG, 31270-901, Brazil*
[c]*Departamento de Química. Universidade Federal do Amazonas, Av. Rodrigo Otávio, 6200 – Coroado, 69077-000 Manaus, AM, Brazil*

(SiO_4) linked through oxygen atoms to one layer of octahedral alumina (AlO_6). The interlayer space is usually filled with water molecules and other ionic species found in the soil.[7,8]

Kaolinite itself is a promising starting material for zeolitic synthesis due to its chemical composition, which contains aluminum and silicon species at a Si/Al ratio of approximately 1. Consequently, hydroxysodalite (SOD), type A (LTA), type X (FAU), and cancrinite (CAN) are the zeolitic phases commonly synthesized from kaolinite.[8–13]

Despite the versatility of their applications, zeolites face a significant limitation in photochemistry due to their large bandgap of >3.0 eV, which renders them insulating materials, particularly in applications such as photocatalysis. Despite this, zeolites are used in photocatalysis as supports for photoactive species or in composite formulations that integrate the high adsorption capacity of zeolites with the photoactivity of other semiconductor materials such as TiO_2, carbon dots, g-C_3N_4, Ag_3PO_4, $BiWO_6$, Fe_2O_3, and others.[14–16]

The combination of zeolites and semiconductor materials offers significant advantages by leveraging the best properties of each material. Zeolites provide a high specific area and high adsorption capacity, which are features that semiconductors lack to be effective photocatalysts. Additionally, the semiconductors can be finely dispersed within the zeolite framework, which may decrease the electron–hole pair recombination rate and increase the atomic active site efficiency of the photocatalyst.[17–19]

Iron oxides, especially hematite (α-Fe_2O_3), are notable visible light responsive and semiconductor materials due to the band gap of 2.0–2.2 eV. However, their efficiency as a photocatalyst is limited by high electron–hole recombination rates. Thus, strategies such as coupling with other semiconductors or downsizing their particles, while dispersing them in a high-specific-area support, are being explored by the scientific community.[20,21]

Junying Wen (2023) and collaborators prepared an Fe-exchanged zeolite β and investigated the photoactivity for degradation of poly- and perfluorinated alkyl substances (PFAS) in water. The authors observed a removal rate from 79 to 100% depending on the substrate (linear or branched) under the investigated conditions. The authors concluded that linear PFAS are most likely to be degraded over the photocatalyst since their adsorption is facilitated.[22]

Guo and collaborators (2024) prepared a composite of carbon dot/TiO_2/zeolite LTA from coal tailing. The authors confirmed the superior activity of the composite which sums the photoactivity of the carbon dots and TiO_2 with the adsorption capacity of the LTA zeolite. Also, the authors suggested that the dispersion of the photoactive materials over the zeolite phase was beneficial for avoiding fast charge recombination in the photocatalyst.[23]

Jan Max and collaborators (2024) prepared Fe-modified zeolites for photodegradation of perfluorooctanoic acid (PFOA). The authors used five commercial zeolites (CHA, MOR, MFI, BEA and FAU) and conducted a post-synthesis modification strategy with Fe^{3+} exchange followed by calcination, which resulted in a finely dispersed iron oxide within the zeolite structures. The authors observed a defluorination rate of up to 60% over Fe-BEA after 240 min. They attributed the material's activity to the generation of $O_2^{\bullet-}$ species on the iron oxide (Fe_2O_3) dispersed within the zeolite framework.[24] Recently, Jian Li and collaborators (2023) synthesized zeolites with extra-large pores and a highly ordered channel system, which can host semiconductor nanoparticles for advanced oxidation processes that transform volatile organic compounds into chemical commodities.[25]

Therefore, the goal of this paper is to investigate the transformation of natural Amazonian kaolinite into photoactive Fe-zeolites and to study their potential application in water treatment for dye removal through photocatalysis by combining the adsorption capacity of zeolites and the photoactivity of the iron oxide species.

2 Materials and methods

2.1 Raw material collection and treatment

The kaolinite sample was collected at Igarapé Cabeça Branca – BR-174 road, km 45 in the direction of Manaus/AM – Boa vista/RR, with geographic coordinates 2°35′8.3″S and 60°1′51.4″W. The collected material was sieved to separate silt and sand (rough fraction) using a 0.065 mm mesh. The smaller particle fraction, $\phi < 0.065$ mm (called KLT), underwent acid treatment with 50% (v/v) HCl at a 1 : 4 (w/v) ratio under 80 °C heating for 4 hours, followed by filtration and washing until pH ~7, and then dried.

2.2 Zeolitic synthesis

Zeolites were synthesized following the method of Ríos and co-workers (2009), which involved two steps: (i) alkaline fusion, where the KLT precursor was macerated with NaOH in a 6 : 5 ratio (w/w) followed by 2 h of heating at 600 °C; and (ii) hydrothermal fusion, where 10 mL of an $Fe(NO_3)_3{\cdot}9H_2O$ solution was slowly added at a concentration of 0.051 mol L^{-1} for 3% (w/w) Fe loading (FeZEO-3) and 0.085 mol L^{-1} for 5% (w/w) Fe loading (FeZEO-5) to the alkaline fusion product. Then, the mixture was magnetically stirred for 6 h at 25 °C and finally transferred to an autoclave at 85 °C for 72 h. After the desired time, the products were collected, washed with distilled water until pH 7, dried in an oven at 100 °C, and stored in a desiccator under vacuum until further use.

2.3 Characterization

Diffractogram patterns were collected in a LabX Shimadzu, model XRD-6000, equipped with a graphite monochromator and copper tube using CuKα radiation, ranging from 5 to 50°/2θ at a step speed of 2 (°/2θ) min^{-1}. Silicon was used as an internal standard. Mössbauer spectra were collected in a spectrometer equipped with a transducer CMTE (model MA250) controlled by a generating unit of linear function CMTE (model MR351) at constant acceleration with ^{57}Co/Rh in the range between ±10 and ±12 mm s^{-1} for 298 and 20 K,

respectively. Data were recorded in 1024 channels and fitted by the least-squares method using Lorentzian curves with WinNormos software. Mössbauer isomer shifts are quoted relative to the α-Fe at room temperature. SEM images were obtained using the microscope of FEI Company, Quanta 250 model, at 30 kV and 40 mA. The band gaps were estimated using diffuse reflectance in the UV region in a UV-2700 spectrometer from Shimadzu equipped with a diffuse reflectance accessory for solids. UV-DRS spectra were collected in a range of 200–800 nm with a 1 nm step. TGA/DTA curves were recorded using DTG-60 from Shimadzu at a N_2 flow rate of 50 mL min^{-1} and a heating rate of 10 °C min^{-1} in the range of 25 to 900 °C.

2.4 Adsorption tests

The adsorption experiments were performed at 25 °C and pH 5.5. Approximately 10 mg of zeolite was added to 10 mL of methylene blue dye in the concentration range of 5 to 50 mg L^{-1} for 60 min. The kinetics studies were performed using approximately 10 mg of catalyst and 10 mL of the dye at a concentration of 40 mg L^{-1} over a time period of 2 to 120 minutes. The concentration of 20 mg L^{-1} was selected for the kinetic studies as it produced the optimal results during the adsorption study. The progress of the adsorption and kinetics was monitored using a UV-vis spectrophotometer (Thermo Scientific, Genesys 106), at a wavelength of 655 nm. Adsorption data were fitted to the following adsorption models.

2.4.1. Langmuir isotherm. The Langmuir empirical model (eqn (1) and (2)) assumes that the active sites where adsorption occurs are energetically homogeneous, forming a monolayer. It also postulates that there is no interaction or steric hindrance between adsorbate molecules, even at adjacent sites. Each adsorbate molecule is assumed to have equivalent adsorption enthalpy and energy, and no transmigration occurs between active sites.

$$Q_{eq} = \frac{Q_{max} b C_e}{1 + bC_e} \quad (1)$$

Linearizing becomes

$$\frac{C_e}{Q_{eq}} = \frac{1}{bQ_{max}} + \frac{C_e}{Q_{max}} \quad (2)$$

where Q_{eq} is the amount of adsorbate adsorbed at equilibrium, Q_{max} is the maximum monolayer coverage capacities, C_e is the adsorbate concentration at equilibrium and b is Langmuir's constant.

2.4.2. Freundlich. This model (eqn (3) and (4)) describes a non-ideal and reversible adsorption process. The coverage surface shows a non-uniform distribution of the energy of the active sites (heat and activity). However, the deviation from Henry's law, especially at lower adsorbate concentrations, makes this model highly criticized.

$$Q_{eq} = K_f C_e^{1/n} \quad (3)$$

Linearly,

$$\log Q_{eq} = \log K_f + \frac{1}{n} \log C_e \quad (4)$$

where Q_{eq} and C_e have the same meaning as described in the Langmuir model, and K_f and n are Freundlich's constants.

2.5 Photocatalytic tests

The photocatalytic activity of the synthesized materials was evaluated against methylene blue organic dye. Initially, 60 mg of the catalyst was mixed with 80 mL of the dye at a concentration of 20 mg L^{-1} for 60 min without radiation incidence to reach adsorption equilibrium. After 60 minutes, the reaction began with the incidence of a UV lamp (15 W), λ = 255 nm, as the light source. The reactions were evaluated by the percentage discoloration (eqn (5)) and monitored every 30 minutes with a UV-vis spectrophotometer (Thermo Scientific, Genesys 106) at a wavelength of 655 nm.

$$\text{Discoloration}\,(\%) = \frac{(C_0 - C_t)}{C_0} \times 100 \quad (5)$$

where C_0 is the solute initial concentration and C_t is the solute concentration at the time t.

The products of the photocatalytic reactions were analyzed using a mass spectrometer (LCQ Finnegan Ion Trap from Thermo Scientific) using electrospray ionization (ESI) in positive mode. Aliquots were injected into the ESI source at a flow rate of 15 L min^{-1}. The capillary temperature was settled at a 275 °C flow rate of the auxiliary gas of 15 mL min^{-1}, a capillary potential of 25 V and 2 kV spray.

3 Results and discussion

3.1 Raw material characterization

The collected kaolinite (KLT-a) has high mineralogical purity, as no significant chemical changes were observed after acid washing (KLT-b) (Table 1). Additionally, only quartz was detected in the XRD pattern alongside the reflections of kaolinite (Fig. 2). The iron oxide content, before and after the chemical treatment, remained approximately 1 wt%, suggesting a possible substitution of Al^{3+} for Fe^{3+} in the crystal lattice of the clay mineral. The presence of iron atoms in the crystalline structure could be expected, given the highly weathered nature of the sampling location.

The thermogravimetric analysis (TGA) of the KLT-b sample shows two major events (Fig. 1). The first occurs in the range of 80–120 °C with an ~2.0% mass loss due to the desorption of water molecules from the material surface. The second and more important event occurs at 510 °C due to the loss of structural hydroxyls in the crystal lattice causing a structural collapse leading to the metakaolin phase. A highly pure and stoichiometric kaolinite has a mass loss of about 14%; thus, it can

Table 1 The chemical composition of the raw material (KLT-a), after acid washing (KLT-b) and the synthesized zeolite samples obtained by XRF

Sample	SiO_2	Al_2O_3	Fe_2O_3	CaO	MgO	TiO_2	Na_2O	K_2O	MnO	LOF[a]
					%(w/w)					
KLT-a	49.4	34.9	1.06	<0.01	<0.1	1.42	<0.1	0.33	<0.01	12.37
KLT-b	48.2	36.7	1.03	<0.01	<0.1	1.40	<0.1	0.29	<0.01	12.86
FeZEO-0	41.4	25.7	0.90	<0.01	<0.1	1.41	16.35	0.15	<0.01	12.38
FeZEO-3	40.1	27.8	1.76	<0.01	<0.1	1.39	13.4	0.12	<0.01	15.01
FeZEO-5	41.7	24.6	2.35	<0.01	<0.1	1.4	12.13	0.14	<0.01	16.45

[a] LOF – loss on fire.

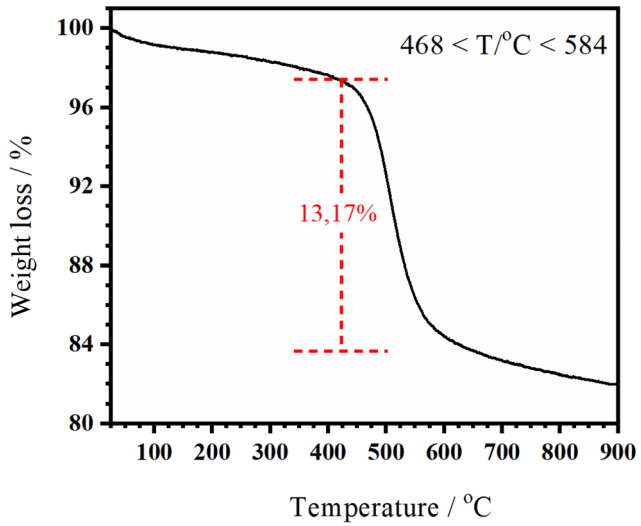

Fig. 1 TGA of the KLT-b sample under a N_2 atmosphere.

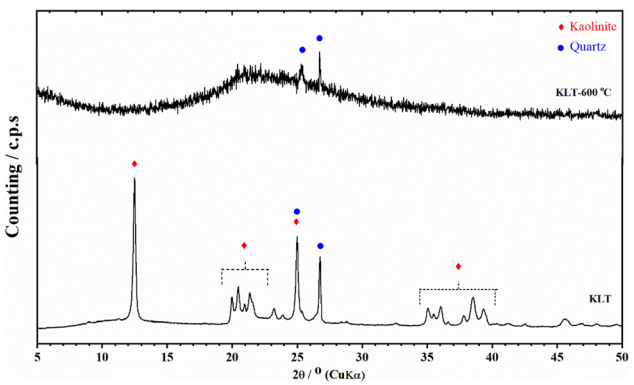

Fig. 2 XRD profile of KLT and KLT after alkaline fusion at 600 °C.

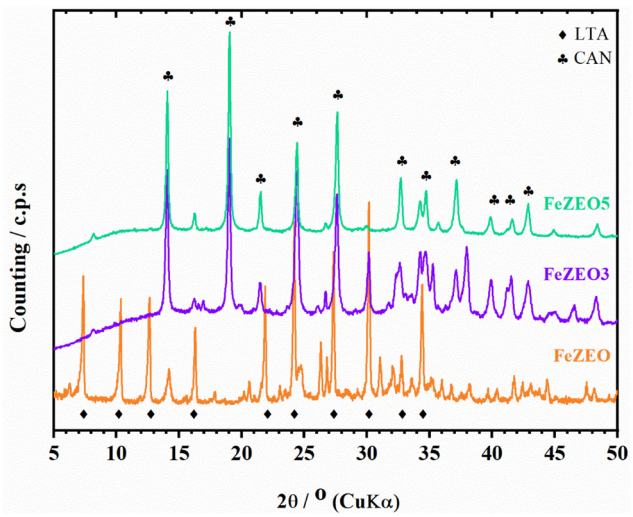

Fig. 3 XRD profiles of FeZEO-0 (green), FeZEO-3 (blue), and FeZEO-5 (orange). Only the main characteristic reflections for LTA and CAN are shown (relative intensity > 50%).

be estimated that a mass loss of 13.17% in KLT-b presents 94% kaolinite purity.[26]

The XRD pattern of the KLT-b sample (Fig. 2) shows mostly kaolinite reflections (card 2290, Mincryst) and quartz trace (SiO_2; card 3895, Mincryst).[27] The alkaline fusion product did not show any kaolinite reflections, and only two quartz reflections could be indexed (Fig. 3), showing that the metakaolinization process was efficient. Kaolinite activation (metakaolinization) is a necessary step in zeolite synthesis from kaolinite due to a change in the aluminum centers octahedrally coordinated to positions of lower spatial symmetry as 4-, 5- and 6-fold, which turns those metallic centers more reactive.[10]

3.2 Zeolite synthesis

The alkaline fusion product was mixed with 10.5 mL solutions of $Fe(NO_3)_3{\cdot}9H_2O$ at 0.051 mol L^{-1} (FeZEO-3) and 0.085 mol L^{-1} (FeZEO-5). The sample labeled FeZEO contained no added $Fe(NO_3)_3$ but retained the natural Fe content present in the raw material. The FeZEO sample resulted in the crystallization of zeolite LTA with traces of SOD zeolite (Fig. 3). Meanwhile, FeZEO-3 and FeZEO-5 XRD patterns completely changed and showed cancrinite (CAN) reflections as the major zeolitic phases zeolite P (GIS) and zeolite hydroxysodalite (SOD) in trace amounts (Fig. 3).[28]

The presence of the zeolitic phases GIS and SOD in trace amounts together with CAN in the samples FeZEO3 and FeZEO5 indicates competing crystallization processes under the synthesis conditions (Fig. 3). As the $Fe(NO_3)_3$ concentration increased from 0% to 3% to 5%, the CAN phase crystalline purity also increased from 0% to 82% to 95%, respectively, estimated by relative areas of the diffractogram (the LTA zeolite reached 96% of crystalline purity in the FeZEO-0 sample). The

global mass yield of the process is between 40% and 50%, determined by comparing the total mass of the kaolinite precursor and NaOH added to the mass of the resulting dry products. Furthermore, the chemical composition of the as-synthesized zeolites LTA and CAN corresponds to the data reported in the literature for zeolites derived from clay minerals[29] (Table 1).

The hydrothermal treatment under autogenic pressure at 85 °C and in the absence of iron(III) nitrate in the reaction media leads mainly to LTA zeolite crystallization (FeZEO-0 sample, Fig. 3). Adding iron(III) nitrate in the solution media of the hydrothermal treatment promotes the reorganization of the amorphous silica and aluminum units into a cancrinite structure with trace amounts of SOD observed in the main reflections at 25.62°, 31.96°, 35.10° and 14.14° (FeZEO-3 sample, Fig. 3) and the virtually pure CAN phase in the FeZEO-5 sample (Fig. 3). Thus, it is hypothesized that the Fe^{3+} cation or the NO_3^- anion might be acting as structural driving agents.

Barnes and coworker (1999) had performed a detailed study about the phase transitions in aluminosilicate by the Bayer process for bauxite beneficiation. The Bayer process consists of ore digestion in a basic solution at a temperature gradient. In other words, a parallel can be done to the synthesis process used in this work.[30] They also observed zeolites like SOD, LTA and CAN in their products. Thus, Barnes established that the medium alkaline conditions and temperature have an important influence on the final zeotype structure.

Krivovichev and collaborators studied the structural complexity of each zeolite structure in the IZA database and found that among the zeolites obtained in this work, the structural complexity increases towards SOD < GIS < LTA; thus, the thermodynamic stability decreases in the reverse order. It is understood that the SOD framework is the most topologically simple among zeolite structures. However, its high structural and chemical flexibility results in a complex behavior in zeolitic phases: intertransformation.[31] Likewise CAN and SOD structures belong to a structural supergroup cancrinite–sodalite of aluminosilicates with AB or ABC-type structures of a 1 : 1 Al : Si ratio. Their structures are based upon layers of 6-membered rings of tetrahedra. Each ring is linked to three rings in the preceding layer and to three rings in the succeeding layer. The simplest frameworks are the 2-layer cancrinite framework (CAN) with the AB sequence and the 3-layer sodalite framework (SOD) with the ABC sequence.[31,32]

Despite the structural correlation of CAN and SOD, the latter being the most thermodynamically stable, the CAN zeolite is most commonly obtained in an alkaline medium under heating in the presence of three folded symmetry anions (C^3 symmetry) such as carbonates and nitrates.[33] Our results corroborate with those observations since the CAN zeolite was only observed in the presence of nitrate salt in the synthesis medium (FeZEO-3 and FeZEO-5). When the NO_3^- concentration is 0% (FeZEO-0), no reflection related to CAN is observed, even at trace levels.

Cancrinite shows a periodic arrangement of small cages (e-cages) distributed in a hexagonal structure with AB–AB stacking. These hexagonal structures are stabilized in the reaction media by NO_3^- anions as observed by LIU and collaborators, 2004 (*Studies in Surface Science and Catalysis*, volume 154). Meanwhile, the LTA zeolite is composed of an arrangement of sodalite cages (or β-cages) interconnected with D4R units. The arrangement of 8 sodalite cages and 12 D4R units forms the α-cage (LTA cages) with an approximate diameter of 11.2 Å and a pore opening of 4.2 Å.

The idealized cell found in the pure silica version of LTA ($Si_{24}O_{48}$) contains one α-cage and one β-cage with lattice parameters of $a = b = c = 11.91$ Å as one can find in the IZA database. However, the aluminum-substituted versions of the LTA zeolite ($Na_x[Al_xSi_{(192-x)}O_{384}]$) which contains 8 α- and 8 β-cages have lattice parameters of $a = b = c = 23.75$–24.55 Å, depending on the aluminum content.[34]

In this work, it was found that the LTA zeolite with a crystallite size of 40.1 nm ((200) plane) and a lattice parameter of a = 23.87 Å (Table 2, FeZEO-0 entry) showed slightly higher values than what are reported in the literature (23.75–24.55 Å), which suggests the existence of some strain effect within the structure caused by the iron naturally present in the kaolinite raw material. Since the ionic radius of tetrahedrally coordinated $_{IV}Fe^{3+}$ = 0.49 Å is higher than the ionic radius of tetrahedrally coordinated $_{IV}Al^{3+}$ = 0.39 Å, a discrete increase in that lattice parameter of the unit cell is expected as observed (Table 2).

Regarding the CAN zeolite diffractogram patterns, a shift in the reflection of the (101) plane to lower reflection angles compared to the IZA standard, from 19.38 2θ/° to 19.02 2θ/° and 19.04 2θ/° for FeZEO3 and FeZEO5 samples, respectively, was observed. This shift may be attributed to the insertion of metallic ions with higher ionic radii (Fe^{3+} in tetrahedral

Table 2 Lattice parameters of FeZEO-0, FeZEO-3 and FeZEO-5

Sample	System	Space group	Lattice parameters		Crystallite size[b] (nm)	Ref.
			a/Å	c/Å		
Siliceous-LTA[a]	Cubic	$Pm\bar{3}m$	11.91	11.91	—	IZA (2025)[28]
Al-substituted-LTA	Cubic	$Pm\bar{3}m$	23.75	23.75	—	Perez-Carbajo (2020)[34]
FeZEO-0	Cubic	$Pm\bar{3}m$	23.87	23.87	40.1	This work
Zeolite CAN[a]	Hexagonal	$P6_3/mmc$	12.49	5.25	—	IZA (2025)[28]
FeZEO-3	Hexagonal	$P6_3/mmc$	12.18	5.17	35.4	This work
FeZEO-5	Hexagonal	$P6_3/mmc$	12.12	5.16	35.1	This work

[a] IZA's standard.[28] [b] Crystallite size in the (100) plane.

coordination) compared to the host elements in the crystalline framework. The strain effect is observed in the change in the apparent shrinkage of ~3% of the lattice parameters of the CAN zeolite (Table 2).

The orange-yellowish color intensity increases in the samples in the order FeZEO-0 > FeZEO-3 > FeZEO-5 which follows the same iron content order in those samples (Fig. 4). This result indicates the existence of iron oxide particles with low crystallinity, finely dispersed in the zeolite material. Besides the crystallinity and the dispersion, the iron content <10% (wt) hinders their detection by XRD analysis. SEM images show particles with a cubic morphology typical of the LTA zeolite on the FeZEO-0 sample (Fig. 4a); meanwhile, images from FeZEO-3 and FeZEO-5 show rod shaped particles from the CAN zeolite (Fig. 4b and c, respectively).

To further investigate the iron distribution in the samples, Mössbauer spectroscopy of ^{57}Fe at 298 and 20 K was performed in order to confirm the isomorphous substitution of Al by Fe and/or crystallization of extraframework iron oxide phases in the zeolitic matrix. The Mössbauer spectrum of FeZEO-5 at 298 K shows a duplet with an isomeric shift, δ = 0.37 mm s^{-1}, and quadrupole splitting, Δ = 0.66 mm s^{-1} of high spin superparamagnetic Fe^{3+} in an octahedral geometry (Fig. 5 and Table 3).

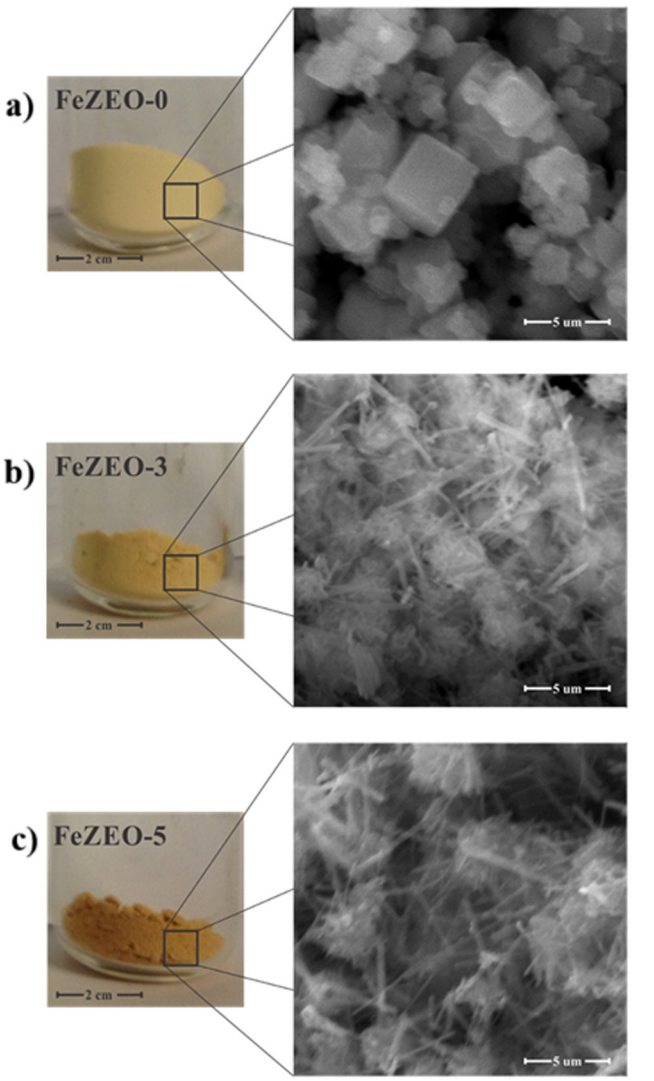

Fig. 4 Color intensification (left) and SEM images (right) of FeZEO-O, FeZEO-3 and FeZEO-5.

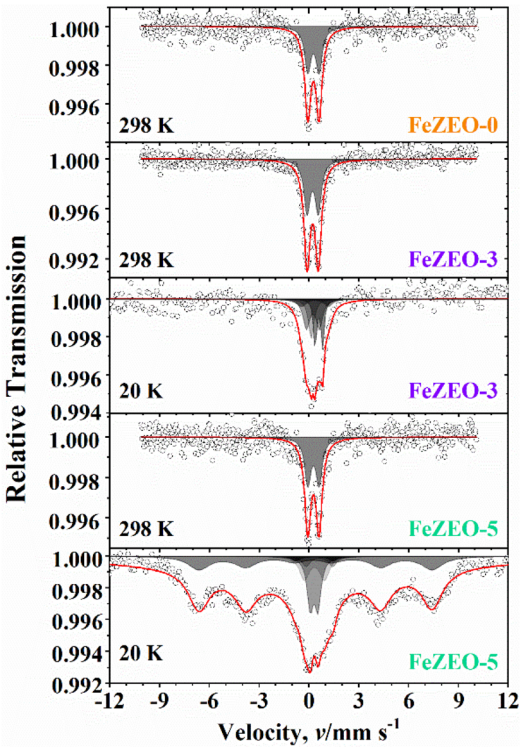

Fig. 5 Mössbauer spectra of the synthesized materials at 298 and 20 K.

Table 3 Mössbauer spectroscopy hyperfine parameters of the raw material and FeZEO-0, FeZEO-3 and FeZEO-5. δ = isomeric shift in relation to α-Fe foil, Δ – quadrupole displacement, ε – quadrupole shift, B_{hf} – hyperfine field and RA – relative area

Sample	Fe^{3+} site	δ/mm s^{-1}	(Δ or ε)/mm s^{-1}	B_{hf}/T	RA/%
298 K					
FeZEO-0	Octahedral	0.36	0.67	—	100
FeZEO-3	Octahedral	0.32	0.65	—	100
FeZEO-5	Octahedral	0.37	0.66	—	100
20 K				—	
FeZEO-3	uncertain	0.70	0.45	—	45.80
	Distorted tetrahedral	0.46	1.60	—	22.46
	Octahedral	0.34	0.77	—	31.74
FeZEO-5	? Fe–O–Si	0.41	0.45	—	15.06
	Distorted tetrahedral	0.63	1.60	—	5.73
	Distorted tetrahedral	0.44	1.21	—	15.68
	Octahedral oligomer	0.44	2.24	—	5.00
	Octahedral	0.43	0.14	43.54	58.53

At low temperatures, it is expected that iron oxide particles start undergoing magnetic coupling, leading to magnetic field splitting between 30 and 45 T. Maghemite (γ-Fe_2O_3) usually shows this behavior as seen in the field distribution profile of FeZEO-5 at 20 K (Fig. 5).[35,36]

Quadrupole splitting ε = 0.14 mm s^{-1} can be seen in the Mössbauer spectrum of FeZEO-5 at 20 K. This value indicates a poorly crystalline maghemite besides having a small particle size (<5 nm). Other Mössbauer subspectra could be fitted on the profile indicating a maghemite partially converted into hematite. The duplet series δ = 0.41 and 0.44 mm s^{-1} and Δ = 0.45 and 2.24 mm s^{-1} show iron sites other than maghemite. Higher quadrupole splitting values shown in Table 3 arise from iron at tetrahedral coordination in the zeolitic lattice, suggesting a degree of isomorphous substitution of Al by Fe in the zeolitic framework.[37] FeZEO-0 and FeZEO-3 hyperfine parameter interpretation may be performed in a similar way.

3.3 Adsorption tests

3.3.1 Adsorption isotherm. The total dye adsorption increased to 21.5% for FeZEO-0, 38.1% for FeZEO-3, and 67.0% for FeZEO-5, respectively. The Langmuir adsorption model was the best fit for all the materials tested, resulting in the affinity parameter 'b' increasing in the following order on the materials: FeZEO-0 < FeZEO-3 < FeZEO-5, as expected since the FeZEO-5 material showed the highest adsorption capacity (Table 4).

The total dye adsorption increased to 21.5, 38.1, and 67.0% for FeZEO-0, FeZEO-3 and FeZEO-5, respectively. Analyzing the statistical parameters R^2, χ^2, and SSE, the Langmuir model provided the best fit for all materials. The Langmuir affinity constant b increased in the order FeZEO-0 < FeZEO-3 < FeZEO-5, consistent with the observation that FeZEO-5 exhibited the highest adsorption capacity (Table 4). The Langmuir model postulates a monolayer adsorption mechanism, in which interactions between adsorbed molecules are negligible.

Table 4 Estimated adsorption parameters for different models and their respective statistical analyses. Experimental conditions: adsorbate = 10 mg, [MB] = 5–50 mg L^{-1}, 25 °C and pH = 5.5

Parameters	FeZEO-0	FeZEO-3	FeZEO-5
Total removal (%)	21.5	38.1	67.0
Langmuir			
Q_{max} (mg g^{-1})	10.14	27.35	42.81
b (dm^3 g^{-1})	0.07	0.11	0.29
R^2	0.9959	0.9853	0.9867
χ^2	1.68	3.84	3.08
SSE	13.5	35.3	32.7
Freundlich			
$1/n$	0.21	1.21	0.45
K_f	6.60	0.61	8.20
R^2	0.7934	0.9332	0.6530
χ^2	120.2	16.9	15.3
SSE	376.1	651.0	256.9

R^2 – linear correlation coefficient using the partial least squares method; χ^2 = nonlinear correlation coefficient; SSE = sum of the squared errors; Q_{max} = maximum adsorption capacity; b, $1/n$, K_f – adsorption constants for each evaluated model.

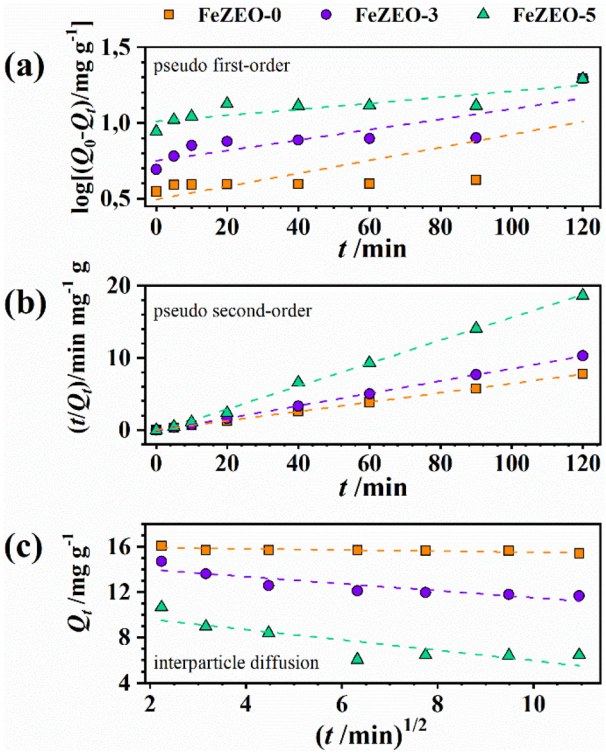

Fig. 6 Kinetic models of (a) pseudo first-order, (b) pseudo second-order and (c) interparticle diffusion of methylene blue dye at a concentration of 40 mg L^{-1}, pH 5.5 at 25 °C for FeZEO-0, FeZEO-3 and FeZEO-5.

3.3.2 Kinetics of adsorption. Experimental kinetic adsorption data were fitted to linearized models: Lagrange pseudo-first-order (Fig. 6a), Elovich pseudo-second-order (Fig. 6b), and intraparticle diffusion (Fig. 6c). All synthesized materials exhibited better fit to the pseudo-second-order kinetics model (eqn (6) and (7)). In heterogeneous adsorption systems, the pseudo-second-order kinetics model may be associated with the adsorption of a single adsorbate molecule onto two distinct adsorption sites.[38–41]

$$\frac{dQ_t}{dt} = K_2 (Q_0 - Q_t)^2 \quad (6)$$

where Q_0 is the initial solute amount in solution, Q_t is the adsorbed solute amount in adsorbent w mass at a t time and K_2 is the adsorption kinetic constant. Integrating eqn (6) into boundary conditions t = 0 to t = t and Q_t = 0 to Q_t = Q_t followed by rearrangement, it becomes eqn (7), being able to set up a $1/Q_t$ *vs.* t graphic.

$$\frac{1}{Q_t} = \frac{1}{K_2 {Q_0}^2} + \frac{1}{Q_0} t \quad (7)$$

where $1/K_2{Q_0}^2$ = intercept of the linearized curves (mg g^{-1} min^{-1}) is the adsorption initial rate.

Table 5 Kinetic adsorption parameters for the pseudo first-order, pseudo second-order and interparticle diffusion models ([MB] = 40 mg L^{-1}, pH 5.5 at 25 °C)

Parameters	FeZEO-0	FeZEO-3	FeZEO-5
Pseudo 1st order			
K_1/min^{-1}	0.0004	0.0014	0.0008
R^2	0.9386	0.7367	0.7392
Pseudo 2nd order			
K_2/(g mg^{-1} min^{-1})	572.95	86.26	15.98
Q_{max}/(mg g^{-1})	6.47	8.65	16.04
R^2	0.999	0.999	0.998
Interparticle diffusion[a]			
K_p/(mg g min$^{1/2}$)	−0.0096	−0.268	−0.443
R^2	0.9732	0.826	0.7222

[a] Data are fitted between 5 and 90 min.

Kinetic studies revealed that FeZEO-0 exhibited the highest kinetic constant (K_2), while FeZEO-5 exhibited the lowest. This trend aligns with the observed adsorption equilibrium times: FeZEO-0 reached equilibrium the fastest (10 min) and exhibited the lowest maximum adsorption capacity (Q_{max} = 6.47 mg g^{-1}). Conversely, FeZEO-3 reached equilibrium in 20 min with a Q_{max} of 8.65 mg g^{-1}, and FeZEO-5 showed the longest equilibrium time (25 min) and the highest Q_{max} (16.04 mg g^{-1}).

While the pseudo-second-order kinetic model exhibited a strong fit, the intraparticle diffusion model (eqn (8)) provides valuable insights. This model demonstrated excellent linearity ($R^2 \approx 1$) within the initial 10–90 minutes of the adsorption process for all synthesized materials. Notably, intraparticle diffusion exerted the greatest influence on FeZEO-0, followed by FeZEO-3 and FeZEO-5 (Table 5), suggesting that it acts concurrently with pseudo-second-order kinetics, potentially as a rate-limiting step during this phase. After 90 minutes, the pseudo-second-order kinetic model appeared to dominate the adsorption process.

$$Q_t = K_p t^{1/2} + C \quad (8)$$

where K_p is the intraparticle diffusion constant rate expressed in mg g^{-1} $min^{0.5}$ and C is the graphical curve intercept.

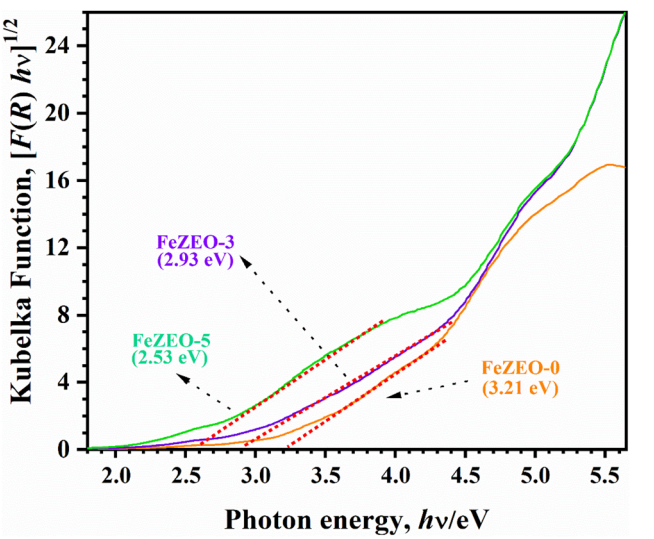

Fig. 7 Kubelka–Munk function plot of indirect allowed transitions estimated through UV-DRS.

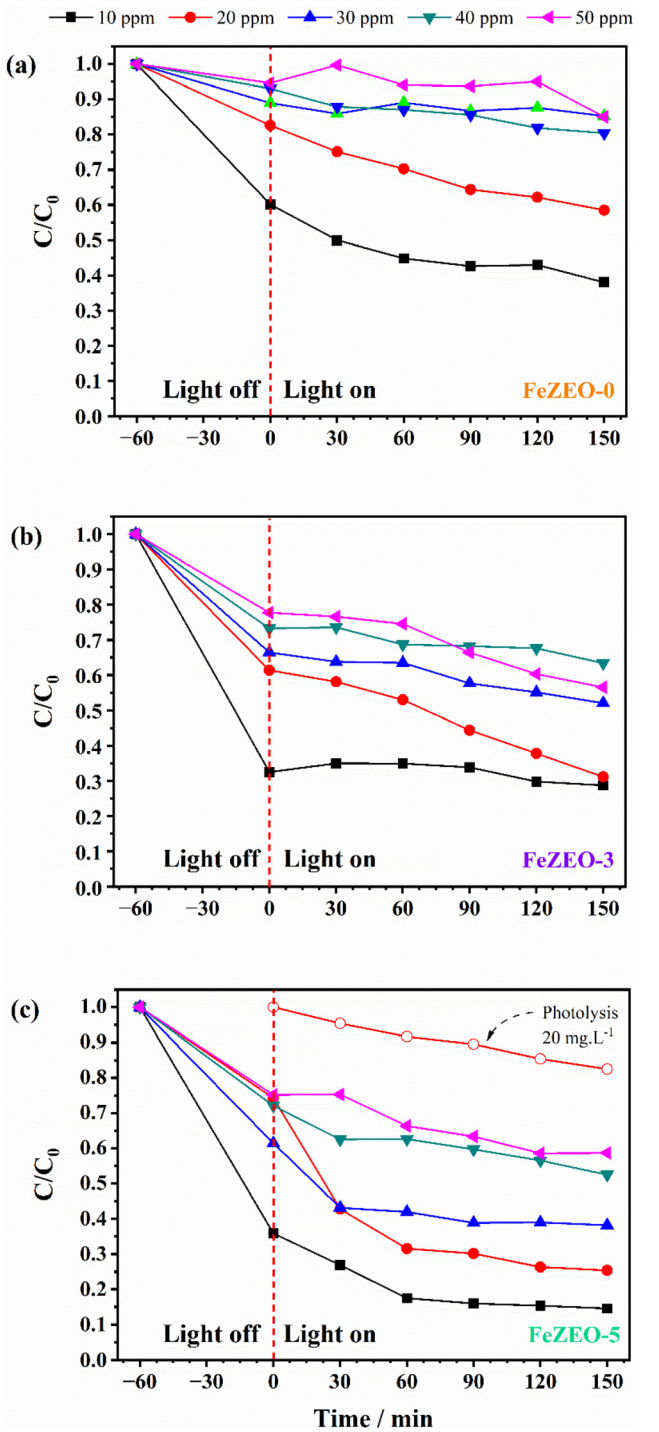

Fig. 8 Dye removal through UV photocatalysis using (a) FeZEO-0, (b) FeZEO-3 and (c) FeZEO-5.

3.4 Photocatalysis

Photocatalytic processes necessitate a compatible bandgap with the incident radiation. The bandgaps of the catalysts were determined by UV-vis diffuse reflectance spectroscopy employing the Kubelka–Munk formalism.[42] Plotting $[F(R)h\nu]^n$ *vs.* $h\nu$ provides an effective approximation of the bandgap (Fig. 7). However, the presence of recombination centers, such as compensation cations, must be considered. Therefore, a material with a low bandgap magnitude (within the range of semiconductor materials) does not inherently guarantee efficient photocatalytic activity.

The indirect transition Kubelka–Munk model (n = 1/2) was employed, which accounts for real-world sampling conditions such as crystalline defects and impurities. These imperfections can introduce permitted energy levels within the bandgap, acting as recombination centers. In indirect transitions, energy released during recombination is transferred to the material structure as phonons.[43] Catalysts synthesized in this study exhibited the most prominent transitions at 3.08 eV, 2.88 eV, and 2.53 eV for FeZEO-0, FeZEO-3, and FeZEO-5, respectively (Fig. 7). The decrease in the band gap is primarily attributed to the increased concentration of iron oxide, which is known to absorb radiation in the UV-vis region. In the maghemite phase (γ-Fe_2O_3), absorption is anticipated at 250 nm, attributed to charge transfer processes, and at 315 nm to 510 nm, corresponding to electronic transitions ($2^6A_1 \rightarrow T, E$).[44] Negative charge accumulation at aluminum centers within the zeolitic framework may shift the Fermi level, facilitating electronic transitions to the conduction band. Bandgap energies determined by UV-DRS suggest that Fe-bearing zeolites may exhibit photocatalytic activity towards methylene blue decolorization.

FeZEO-5 exhibited the highest methylene blue (MB) removal efficiency at all investigated concentrations, followed by FeZEO-3 and lastly FeZEO-0 (Fig. 8). Kinetic studies indicated that both adsorption and photocatalysis contribute to dye removal, as these processes are inherently intertwined. The higher iron content in FeZEO-5 led to a narrower bandgap, facilitating radical generation *via* two primary mechanisms: (i) dissolved oxygen reduction to superoxide ($O_2^{\bullet -}$), which subsequently reacts with H^+ to form hydroperoxyl radicals ($HOO^\bullet$) and rapidly decomposes to hydroxyl radicals ($HO^\bullet$); and (ii) direct oxidation of hydroxide ions (OH^-) according to reactions (1)–(6).[45] FeZEO-0 exhibited negligible photocatalytic activity, with MB removal primarily attributed to adsorption. The optimal system for photocatalytic MB degradation was achieved with a 20 mg L^{-1} MB concentration and FeZEO-5 as the catalyst, resulting in a 75% total removal yield. A control experiment, conducted under the same conditions but without a catalyst, accounted for 18% removal due to photolysis of methylene blue (Fig. 8c). At higher MB concentrations (>30 mg L^{-1}), adsorption dominated over photocatalysis, resulting in negligible observable photoactivity.

$$Fe_2O_3 \text{ or Fe-zeolite} + h\nu \rightarrow Fe_2O_3(e_{cb}^-, h_{vb}^+) \quad (1)$$

$$Fe_2O_3(h_{vb}^+) + H_2O_{ads} \rightarrow Fe_2O_3 + HO^\bullet_{ads} + H^+ \quad (2)$$

$$Fe_2O_3(h_{vb}^+) + HO_{ads}^- \rightarrow Fe_2O_3 + HO^\bullet_{ads} \quad (3)$$

$$Fe_2O_3(h_{vb}^+) + Substrate_{ads} \rightarrow Fe_2O_3 + Substrate_{ads}^+ \quad (4)$$

$$HO^\bullet + Substrate_{ads} \rightarrow Substrate_{oxid} \quad (5)$$

$$Fe_2O_3(e_{cb}^-) + Substrate_{ads} \rightarrow Fe_2O_3 + Substrate_{ads}^- \quad (6)$$

To investigate the photocatalytic activity, aliquots of the FeZEO-5 reaction were analyzed by electron spray ionization mass spectrometry (ESI-MS). Prior to irradiation, the primary peak observed in the mass spectrum corresponded to the methylene blue cation (m/z = 284). After 150 minutes of irradiation, new peaks with m/z 302 and 318 were detected, which are likely attributed to successive hydroxylation products resulting from $^\bullet$OH radical attack on the methylene blue molecule (Fig. 9). The peak at m/z 274 suggests that the mechanism of MB degradation may also proceed *via* a demethylation route, while the peak at m/z 385 suggests the formation of strongly oxidized products resulting from oxidation of the S and/or N heteroatoms on the native MB structure.[46–48]

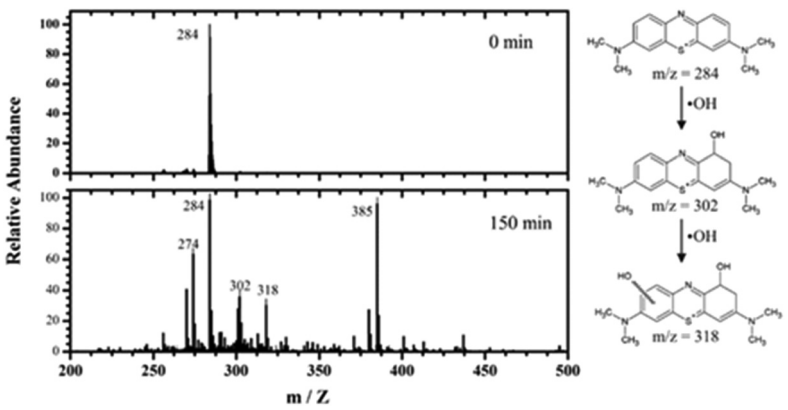

Fig. 9 ESI-(+)-MS of standard methylene blue at 0 min and after 150 min reactions with FeZEO-5 under UV irradiation.

4 Conclusion

An Fe-CAN zeolite was successfully synthesized from kaolinite utilizing $Fe(NO_3)_3$ as both a doping agent and a structure-directing agent. Iron species were predominantly present as maghemite, although some iron atoms were likely incorporated into the zeolite framework. In the absence of iron salt in the reaction media, an LTA zeolite was obtained.

Kinetic studies demonstrated that methylene blue removal by FeZEO-0, FeZEO-3, and FeZEO-5 was best described using the pseudo-second-order kinetic model. The Langmuir isotherm provided the most suitable fit for all samples, with FeZEO-5 (cancrinite containing maghemite) exhibiting the highest adsorption capacity (16.04 mg g^{-1}). Intraparticle diffusion was observed to be the rate-controlling step during the initial 90 minutes of adsorption.

FeZEO-5 demonstrated superior methylene blue (MB) removal efficiency in photocatalytic processes compared to FeZEO-3 and FeZEO-0. This enhanced performance is attributed to a synergistic effect: the cancrinite zeolite framework facilitated dye adsorption, while the higher iron content in FeZEO-5 narrowed the bandgap of the photocatalyst. This bandgap narrowing led to an increased generation of reactive radical species, which effectively degraded the pre-adsorbed MB molecules. Evidence for this includes the formation of hydroxylated MB degradation products.

This study demonstrates that Amazonian kaolinite can be effectively transformed into zeolites, with the nitrate anion serving as a structure-directing agent in zeolite synthesis. The resulting maghemite–cancrinite composite exhibits both adsorption capacity and photoactivity under UV irradiation for MB removal.

Author contributions

Victor Augusto Araújo de Freitas: conceptualization, writing – original draft and supervision. Débora de Souza Pinheiro: investigation and formal analysis. Camila Ferreira Peixoto: investigation and formal analysis. Luiz Carlos Alves de Oliveira: funding acquisition and writing – review & editing. Paulo Rogério da Costa Couceiro: funding acquisition and writing – review & editing.

Data availability

The authors guarantee that all data presented in this article are original and are available for access when requested by the reader. If necessary, please contact the corresponding author.

Conflicts of interest

There are no conflicts to declare.

Acknowledgements

The authors thank CNPq for scholarship granting and the Laboratório de Análises Mineralógicas at the Geoscience Department of the Federal University of Amazonas for SEM images.

References

1 C. Han, J. Yang, S. Dong, L. Ma, Q. Dai and J. Guo, *Sep. Purif. Technol.*, 2025, **354**, 128957.
2 L. Ma, Y. Li, Q. Wang, N. Feng, R. Wang, M. Yang, Q. Ma, Y. Li, Y. Ma, Y. Sun, X. Ma and W. Ji, *J. Mater. Chem. A*, 2025, **13**(10), 7324–7334.
3 P. Yan, H. Peng, J. Vogrin, H. Rabiee and Z. Zhu, *J. Mater. Chem. A*, 2023, **11**, 17938–17960.
4 X. Chen, P. Zhang, Y. Wang, W. Peng, Z. Ren, Y. Li, B. Chu and Q. Zhu, *Front. Environ. Sci. Eng.*, 2023, **17**, 149.
5 X. Chen, S. Zhou, X. Zhang, S. Chen, L. Wang, C. Zhang, S. Gao, D. Yu, X. Fan, Y. Cheng, Y. Zhang, X. Yu and Z. Zhao, *J. Mater. Chem. A*, 2024, **12**, 16293–16328.
6 M. Feng, Z. Kou, C. Tang, Z. Shi, Y. Tong and K. Zhang, *Appl. Clay Sci.*, 2023, **243**, 107087.
7 I. El Bojaddayni, M. E. Kuçuk, Y. El Ouardi, I. Jilal, S. El Barkany, K. Moradi, E. Repo, K. Laatikainen and A. Ouammou, *Miner. Eng.*, 2023, **198**, 108086.
8 Q. Zheng, Z. Wang, Z. Tian, L. Cai, C. Jiang, L. Deng, D. Yang and Z. Wei, *Chem. Eng. J.*, 2025, 160616.
9 J. A. Cecilia, E. Vilarrasa-García, R. Morales-Ospino, E. Finocchio, G. Busca, K. Sapag, J. Villarroel-Rocha, M. Bastos-Neto, D. C. S. Azevedo and E. Rodríguez-Castellón, *Fuel*, 2022, **320**(15), 123953.
10 A. Rahman, A. Purwanto, A. Endah, E. Handoko, E. Kusrini and E. A. Prasetyanto, in *Journal of Physics: Conference Series*, IOP Publishing Ltd, 2019, vol. 1402.
11 P. R. dos Santos de Castroa, A. Á. B. Maia and R. S. Angélica, *Mater. Res.*, 2019, **22**(5), DOI: **10.1590/1980-5373-mr-2019-0321**.
12 J. Vogrin, T. Santini, H. Peng, L. Zhao and J. Vaughan, *Appl. Clay Sci.*, 2023, **244**, 107106.
13 N. Sazali, Z. Harun, T. Abdullahi, F. H. Azhar, A. Ahmad, N. I. Rasli and N. Sazali, *Biointerface Res. Appl. Chem.*, 2022, **12**, 7376–7393.
14 Y. Guo and B. Zu, *J. Thermodyn. Catal.*, 2012, **4**, 2.
15 A. Corma and H. Garcia, *Chem. Commun.*, 2004, **4**, 1443–1459.
16 G. Ferraro, A. Di Vera, E. Ghedini, M. Marchiori, G. Forghieri, P. Canton and M. Signoretto, *Appl. Catal. O: Open*, 2024, **192**, 206942.
17 F. S. de Dios, E. R. Morales, M. del Carmen Arellano Cortaza, G. P. Hernández, E. V. M. Mandujano, E. M. L. Alejandro and L. R. Blanco, *Desalin. Water Treat.*, 2023, **312**, 79–88.

18 I. Liaquat, R. Munir, N. A. Abbasi, B. Sadia, A. Muneer, F. Younas, M. F. Sardar, M. Zahid and S. Noreen, *Environ. Pollut.*, 2024, **349**, 123922.
19 J. Guo, Y. Fan, X. Dong, H. Zeng, X. Ma and Y. Fu, *J. Environ. Manage.*, 2024, **354**, 120342.
20 A. Balapure, J. Ray Dutta and R. Ganesan, *RSC Appl. Interfaces*, 2024, **1**, 43–69.
21 L. El Gaini, *Desalin. Water Treat.*, 2024, **320**, 100798.
22 J. Wen, H. Li, L. D. M. Ottosen, J. Lundqvist and L. Vergeynst, *Chemosphere*, 2023, **344**, 140344.
23 J. Guo, Y. Fan, X. Dong, H. Zeng, X. Ma and Y. Fu, *J. Environ. Manage.*, 2024, **354**, 120342.
24 J.-M. Arana Juve, X. Baami González, L. Bai, Z. Xie, Y. Shang, A. Saad, R. Gonzalez-Olmos, M. S. Wong, M. Ateia and Z. Wei, *Appl. Catal., B*, 2024, **349**, 123885.
25 J. Li, Z. R. Gao, Q.-F. Lin, C. Liu, F. Gao, C. Lin, S. Zhang, H. Deng, A. Mayoral, W. Fan, S. Luo, X. Chen, H. He, M. A. Camblor, F.-J. Chen and J. Yu, *Science*, 2023, **379**, 283–287.
26 M. Izadifar, P. Thissen, A. Steudel, R. Kleeberg, S. Kaufhold, J. Kaltenbach, R. Schuhmann, F. Dehn and K. Emmerich, *Clays Clay Miner.*, 2020, **68**, 319–333.
27 Mincryst, **https://database.iem.ac.ru/mincryst/**.
28 IZA, Internacional Zeolite Association, **https://www.iza-structure.org/databases/**, (accessed 14 May 2024).
29 M. Feng, Z. Kou, C. Tang, Z. Shi, Y. Tong and K. Zhang, *Appl. Clay Sci.*, 2023, **243**, 107087.
30 M. C. Barnes, J. Addai-Mensah and A. R. Gerson, *Microporous Mesoporous Mater.*, 1999, **31**, 287–302.
31 S. V. Krivovichev, *Microporous Mesoporous Mater.*, 2013, **171**, 223–229.
32 J. Antúnez-García, D. H. Galván, V. Petranovskii, F. N. Murrieta-Rico, R. I. Yocupicio-Gaxiola, M. G. Shelyapina and S. Fuentes-Moyado, *Comput. Mater. Sci.*, 2021, **196**, 110557.
33 F. Ocanto, R. Álvarez, C. Urbina de Navarro, A. Lieb and C. F. Linares, *Microporous Mesoporous Mater.*, 2008, **116**, 318–322.
34 J. Perez-Carbajo, S. R. G. Balestra, S. Calero and P. J. Merkling, *Microporous Mesoporous Mater.*, 2020, **293**, 109808.
35 H. Abbas, A. D. Manasrah, A. A. Saad, K. O. Sebakhy and Y. Bouhadda, *Pet. Chem.*, 2021, **61**, 67–75.
36 B. Abdelwahab, G. S. M. Ahmed, M. El-Ghazaly, A. Zoulfakar and S. M. Salem, *Ann. Nucl. Energy*, 2024, **198**, 110292.
37 C. Kosanoviü, S. Bosnar, B. Subotiü, K. Lázár and N. Novak, in Proceedings of 4th International FEZA Conference, 2008, pp. 929–932.
38 B. G. Cho, K. Y. Lee, S. B. Mun, C. R. Lim, Y. S. Yun and C. W. Cho, *Ecotoxicol. Environ. Saf.*, 2024, **270**(15), 115869.
39 M. E. S. Pedebos, D. M. Druzian, L. R. Oviedo, Y. P. M. Ruiz, A. Galembeck, G. Pavoski, D. C. R. Espinosa and W. L. da Silva, *J. Photochem. Photobiol., A*, 2024, **449**(1), 115404.
40 H. G. Quynh, H. Van Thanh, N. T. T. Phuong, N. P. T. Duy, L. H. Hung, N. Van Dung, N. T. H. Duong and N. Q. Long, *Environ. Technol. Innovation*, 2023, **31**, 103155.
41 M. T. Ritter, M. Á. Lobo-Recio, I. Padilla, M. E. Nagel-Hassemer, M. Romero and A. López-Delgado, *J. Ind. Eng. Chem.*, 2024, **136**(25), 177–187.
42 M. Knezevic, V.-D. Quach, I. Lampre, M. Erard, P. Pernot, D. Berardan, C. Colbeau-Justin and M. N. Ghazzal, *J. Mater. Chem. A*, 2023, **11**, 6226–6236.
43 P. F. Wang, Z. H. Li and Y. M. Zhu, *Mater. Chem. Phys.*, 2010, **123**, 356–359.
44 R. M. Cornell and U. Schwertmann, *The Iron Oxides*, Wiley, 2003.
45 L. Yang, Z. Chen, Q. Cao, H. Liao, J. Gao, L. Zhang, W. Wei, H. Li and J. Lu, *Adv. Mater.*, 2024, **36**, 3.
46 W. Zhang, D. Liu, Z. Mu, X. Zhang, G. Dong, L. Bai, R. Guo, J. Li, M. Zhao and Z. Zhang, *J. Inorg. Organomet. Polym. Mater.*, 2023, **33**, 90–104.
47 D. Matsunami, K. Yamanaka, T. Mizoguchi and K. Kojima, *J. Photochem. Photobiol., A*, 2019, **369**, 106–114.
48 L. Wu, Q. Xie, Y. Lv, Z. Zhang, Z. Wu, X. Liang, M. Lu and Y. Nie, *RSC Adv.*, 2019, **9**, 25967–25975.